NDT&E International 146 (2024) 103160

Contents lists available at ScienceDirect

NDT and E International

journal homepage: www.elsevier.com/locate/ndteint

Research Paper

Flexible anisotropic magnetoresistive sensors for novel magnetic flux leakage testing capabilities

Alberto Nicolicea [a,*], Eduardo Sergio Oliveros-Mata [b], Yevhen Zabila [b], Denys Makarov [b], Michael Melzer [a], Matthias Pelkner [a]

[a] Bundesanstalt für Materialforschung und -prüfung, Division 8.4 Acoustic and Electromagnetic Methods, Unter den Eichen 87, Berlin 12205, Germany
[b] Helmholtz-Zentrum Dresden-Rossendorf e.V., Institute of Ion Beam Physics and Materials Research, Bautzner Landstraße 400, Dresden 01328, Germany

ARTICLE INFO

Keywords:
Magnetic field sensors
Flexible magnetic field sensors
Flexible electronics
Non-destructive testing
Magnetic flux leakage
Thin film sensor fabrication
Defect detection
Magnetism

ABSTRACT

Rigid magnetic field sensors such as anisotropic magnetoresistive (AMR), giant magnetoresistive (GMR) and Hall sensors have been used for years and have become industry standard for electromagnetic non-destructive testing (NDT). Recent technological developments in the field of flexible electronics allow for the fabrication of reshapeable magnetic field sensors on flexible substrates via thin-film deposition or printing. The magnetic properties of these sensors have comparable characteristics to industry-standard rigid magnetic field sensors, with the added ability of adapting to the surface of complex components and scanning in contact with the sample surface. This improves defect detectability and magnetic signal strength by minimizing the scanning lift-off (LO) distance. In this article flexible AMR sensors mounted on a rotative mechanical holder were used to scan a semi-circular ferromagnetic sample with 3 reference defects via magnetic flux leakage (MFL) testing, thus demonstrating the applicability of this type of sensors for the scanning of curved samples. In order to benchmark the performance of these sensors in comparison to industry standard rigid magnetic field sensors, a ferromagnetic sample with 10 reference defects of different depths was scanned employing flexible AMR and rigid GMR sensors. Defects with depths ranging from 110 μm up to 2240 μm were detected with an signal-to-noise ratio (SNR) of 2.7 up to 27.9 (for flexible AMR sensors) and 6.2 up to 72.3 (for rigid GMR sensors), respectively. A 2D magnetometer mapping of the sample with a spatial scanning step of 10×50 μm^2 (flexible AMR) and 16×100 μm^2 (rigid GMR) was obtained. The results show that this type of sensor can be used for high-resolution and high-detail mapping of defects on the surface of planar and non-planar ferromagnetic samples since the scanning lift-off distance is equal to the substrate thickness of 20 μm for in-contact scanning. The SNR comparison between flexible and rigid sensors shows that the performance of the flexible AMR sensors employed is not very far behind the performance of the rigid GMR sensors used.

1. Introduction

Non-destructive testing (NDT) methods are essential for investigating the integrity and quality of components or products without destroying or damaging them. The objective is to detect cracks, defects or material anomalies on or close to the surface of the components to be inspected [1]. Common strategies employed for evaluating the structural integrity of ferromagnetic samples include magnetic particle inspection (MPI) using ferritic powders and magnetic flux leakage testing (MFL) using magnetic field sensors. These methods are widely used in industry for quality control and fault inspection [2,3].

When a magnetized sample has a sudden discontinuity in its geometry or magnetic properties, magnetic field lines from within the magnetized bulk material leak out of the sample locally [4]. This typically happens in the regions where defects or cracks are present. These local magnetic fields are known as stray fields (SF). These SF can only be detected near the surface, since their strength decreases strongly with the lift-off (LO) distance – which corresponds to the distance between the sensitive layer of the sensor and the sample surface – due to the dispersive nature of magnetic fields [5].

For MFL testing, the component to be inspected is magnetized globally prior to scanning or locally during scanning by adjacent coils, yokes or permanent magnets [6]. As a consequence, the sample emits a background bias field from its magnetic poles when globally magnetized, or locally when partially magnetized [7]. The effect of this field can be eliminated by processing the experimental data, or by employing differential sensors or coils, thus isolating the signal corresponding to the SF emitted by defects.

* Corresponding author.
E-mail address: alberto.nicolicea@bam.de (A. Nicolicea).

https://doi.org/10.1016/j.ndteint.2024.103160
Received 27 November 2023; Received in revised form 5 April 2024; Accepted 8 June 2024
Available online 12 June 2024

The standard MFL testing method used in industry to investigate the surface of ferromagnetic components or materials is MPI. This procedure relies on visualizing the magnetic flux by using phosphorescent magnetic particles which are attracted by the SF of defects and accumulate around them [8]. This method is sensitive to small magnetic fields, besides being simple and straightforward to implement.

However, this technique provides only a general qualitative mapping and localization of defects and cracks and not a quantitative analysis of the magnetic profile of these defects. Furthermore, it is not an easy method to automatize and thus most testing is done manually, although in recent years there have been effort to improve the procedure using artificial intelligence (AI) for optical inspection [9]. In contrast to MPI, the scanning of SF employing magnetic field sensors provides a quantitative analysis of the magnitude and profile of the measured stray fields. In addition, this method also provides the capability of detecting sub-surface or hidden defects [10,11].

The most commonly used sensors in industry for the detection of SF are Hall sensors and flux-gates (the latter have a lower spatial resolution but higher sensitivity to magnetic fields compared to Hall sensors), together with magneto-resistive (MR) sensors [12]. These devices have been employed in several applications ranging from aircraft component inspection to the inspection of power grid overhead transmission lines and underground power cables [13].

Previous work done in this field has explored the application of rigid giant magnetoresistive (GMR) sensors for non-destructive magnetic flux leakage testing for the measuring of defects with dimensions down to the order of hundreds of μm [14–24]. These sensors can also be used to scan circular ferromagnetic bearings [25].

Although this method of using rigid magnetic field sensors to scan samples provides a quantitative analysis of surface defects, it faces the challenge of scanning complex surfaces. An air-gap (of the order of hundreds of μm) must be maintained between the sensors and the sample in order not to damage either. Therefore, the scanning of complex surfaces of any arbitrary shape requires a complex automatized system to ensure the proper scanning distance.

In this area, the current MFL technology is mostly focused on the detection of defects along steel wire ropes and pipes, due to its high demand from industry [26–33]. Permanent magnets or yokes are normally used to magnetize the material during scanning along the length of the wire, with the flaw detection being generally done employing Hall sensors.

The scanning methods used in this case suffer from the same limitation of requiring a LO distance between the sensors and yokes or magnets and the steel pipe or wire surface. This distance also varies since the sensors are not conformal to the irregular sample surface. Previous attempts to fix these issues were performed by scanning steel track ropes using rigid GMR sensors mounted on a flexible printed circuit board (PCB) [34]. However, in this case the rigid sensors were still not intrinsically conformal to the surface, and for samples with small radius this would affect the results.

To address these limitations and simplify the scanning process, we propose the employment of flexible magnetic field sensors for NDT measurements, which are the product of recent developments in flexible electronics. These flexible magnetic field sensors produced by thin-film deposition on flexible substrate show promising capabilities for several applications such spatial navigation, micro-fluidic particle detection, biomedical applications and intelligent textiles [35–41]. Therefore it is of interest to study the applications of these devices to electromagnetic NDT testing, since it would enable the scanning of surfaces with any arbitrary shape.

These conformal sensors offer unique advantages, including the ability to conduct close-range in contact scanning without risking damage to samples or sensors. This reduces the scanning lift-off (LO) distance down to the flexible substrate thickness (20 μm for Kapton foils, 2 μm for Mylar foils). This feature promises an enhancement of the detected SF signal strength by 1-2 orders of magnitude, since the circular nature of stray fields implies that the clearest mapping is obtained close to the surface. This signal strength increase is illustrated in Fig. 1. The inset shows the proposed method for MFL scanning using flexible magnetic field sensors.

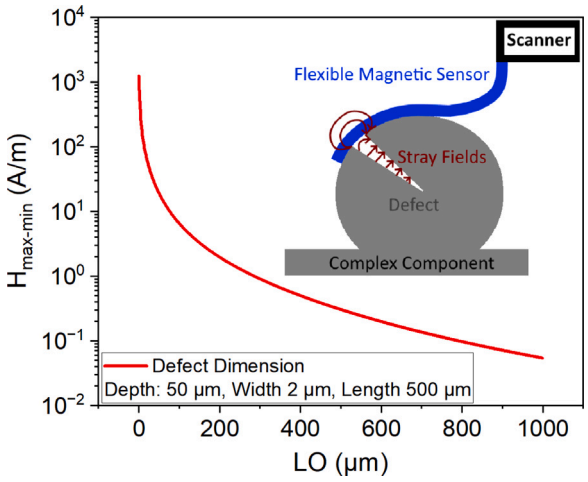

Fig. 1. Simulated data for the signal amplitude of the stray field emanating from a defect with specific dimensions, showing a potential 1-2 order of magnitude increase in signal magnitude when scanning close to the sample surface. Inset exemplifying the proposed scanning method with flexible magnetic field sensors.

Furthermore, in-contact scanning also promises the capacity to collect detailed information about the sample surface such as the presence of irregularities in the magnetic material resulting from residual stress, hardness or material changes that have a magnetic flux leakage signature [42,43]. These features would not be detectable farther away from the surface. Finally, the flexibility of these devices would enable the scanning of complex surfaces, such as those produced by novel additive manufacturing methods, while demonstrating performance for defect detection on both planar and non-planar surfaces.

In this article flexible anisotropic magnetoresistive (AMR) sensors mounted on a rotative mechanical holder were used to scan a semi-circular ferromagnetic sample with 3 reference defects via magnetic flux leakage (MFL) testing, thus demonstrating the applicability of this type of sensors for the scanning of curved samples.

In order to benchmark the performance of these sensors in comparison to industry standard rigid MR sensors, a ferromagnetic sample with 10 reference defects of different depths was scanned employing flexible AMR and rigid GMR sensors. Defects with depths ranging from 110 μm up to 2240 μm were detected with an signal-to-noise ratio (SNR) of 2.7 up to 27.9 (for flexible AMR sensors) and 6.2 up to 72.3 (for rigid GMR sensors), respectively. A 2D magnetometer mapping of the sample with a spatial scanning step of 10×50 μm^2 (flexible AMR) and 16×100 μm^2 (rigid GMR) was obtained.

The results show that this type of flexible sensors can be used for high-resolution and high-detail mapping of defects on the surface of planar and non-planar ferromagnetic samples since the scanning LO distance is equal to the substrate thickness of 20 μm. This enables in-contact scanning, at a distance much closer to the sample surface when compared to measurement distance of 200 μm used in the case of rigid GMR scanning.

The SNR comparison between flexible and rigid sensors shows that the performance of the flexible AMR sensors employed is not far behind the performance of the rigid GMR sensors used. Moreover, these flexible sensors uncover magnetic signatures that are observable only upon direct contact with the sample during scanning.

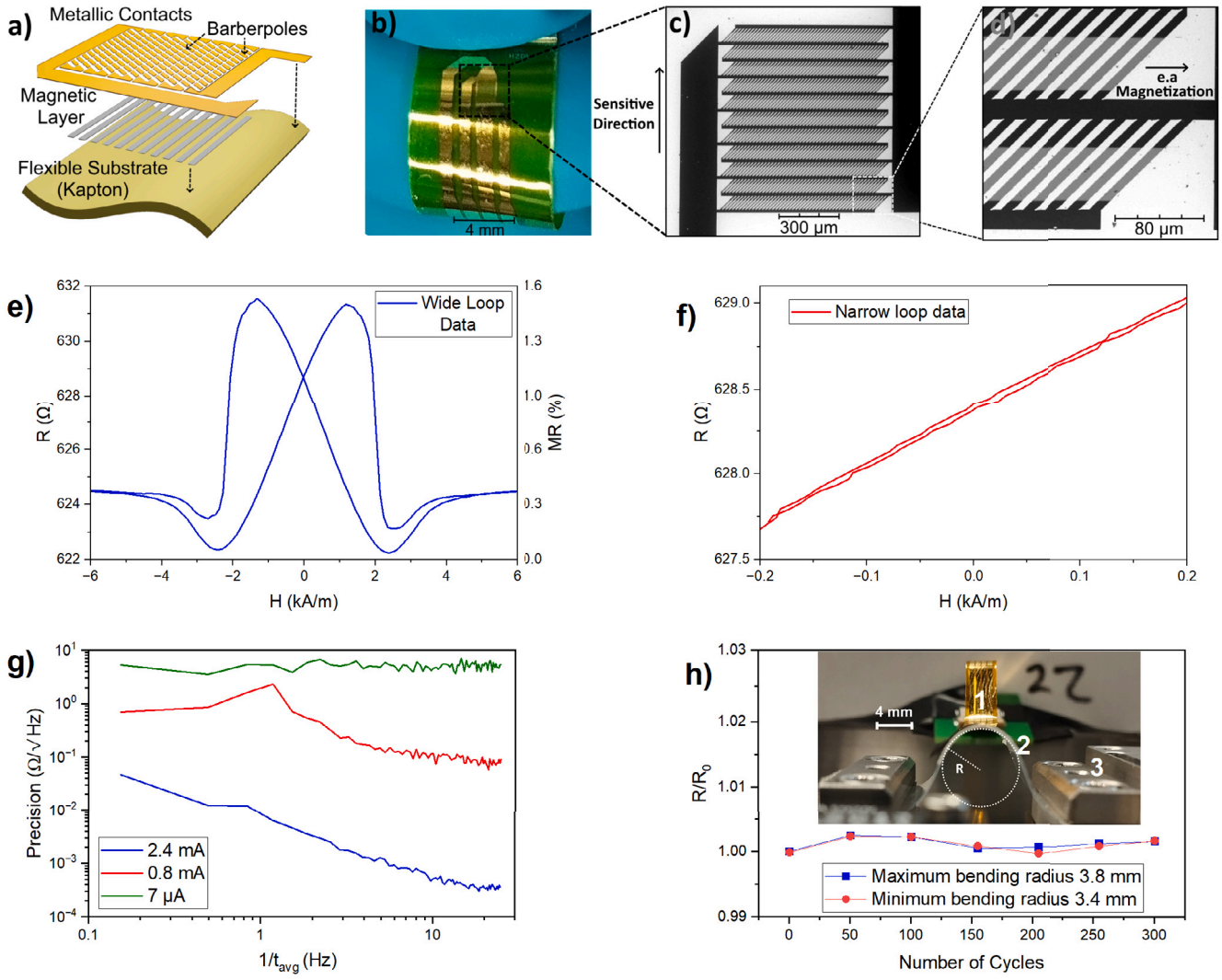

Fig. 2. Flexible AMR sensor overview: (a) The magnetic layer [Py 100 nm] of the AMR sensor is deposited on a flexible substrate (Kapton, thickness 20 µm); this is followed by the deposition of a metallic layer [Au 100 nm] forming the barber-pole structure and the electrical contacts. (b) Photography demonstrating the flexibility of the sensor. (c) Scanning electron microscopy (SEM) of the sensitive region of the sensor (1×1 mm^2). The sensitive direction of detection is also shown. (d) SEM image showing a more detailed image of the magnetic bars and the metallic barber-poles deposited on top. (e) Magnetic characterization in the sensitive range [−6;6] kA/m with a corresponding magnetoresistance of 1.5%. (f) Narrow loop magnetic characterization around zero field value, displaying the linearity of the sensor in that region. (g) Electrical noise characterization for several values of current; at the current of 2.4 mA, the sensor is only stable for measurements above 10 Hz corresponding to measurement times lower than 100 ms. (h) Mechanical cyclic testing characterization showing the sensor resistance variation as a function of the number of bending cycles for the bending radius range of [3.4; 3.8] mm. Inset displaying the characterization setup employed: AMR sensor (1) glued to the surface of the bendable plastic surface (2). Mechanical device (3) moving cyclically within a certain range.

2. Flexible AMR sensors

In the flexible linear AMR sensors employed in this article, geometric anisotropy in the design of the magnetic bars of the sensors leads to a alignment of magnetization which tilts when exposed to an external magnetic field. The varying angle between the magnetization direction and the current flow leads to a change in the electrical resistance of the sensor, which can then be measured [44].

These sensors were fabricated with standard thin-film fabrication processes:

Handling glass slides were coated with Polydimethylsiloxane (PDMS, Sylgard 184, ratio 1:10) via spin coating at 1000 r.p.m. for 30 s and cured at 80 °C for 60 min. A Kapton substrate with a thickness of 20 µm was attached to the coated glass slides, thus ensuring that the flatness of the flexible substrate is maintained during the fabrication process.

Afterwards, Photolithography was conducted over the Kapton foils using AZ5214e photoresist (Microchemicals GmbH, Germany) spun at 3000 r.p.m. for 30 s and cured at 110 °C for 2 min. The pattern exposure was performed using a direct laser writer (DWL66 — Heidelberg Instruments Mikrotechnik GmbH, Germany) and the sensors were afterwards developed for 30 s in AZ324B developer (Microchemicals GmbH, Germany).

A layer of 100 nm Permalloy (Py) was deposited on the substrate via e-beam evaporation (pressure: 8×10^{-4} mbar). After material removal using acetone, the magnetic layer is obtained, as shown in Fig. 2(a).

In the next step, a 5-nm-thick adhesion layer of chromium (Cr) was again deposited by e-beam evaporation (pressure: 8×10^{-4} mbar), followed by deposition of a 100-nm-thick layer of gold (Au) (pressure: 8×10^{-4} mbar). After material removal using acetone, the metallic layer is obtained. The resulting sensors are shown in Fig. 2(b).

The design of the magnetic layer then consists of 11 magnetic bars of dimensions 1000×50 µm^2 each, forming a sensing area of (1×1 mm^2) as shown in Fig. 2(c). The shape anisotropy arising from the ratio between the length L and width W of these structures gives the sensor its magnetic properties. The ratio L:W is equal to 20.

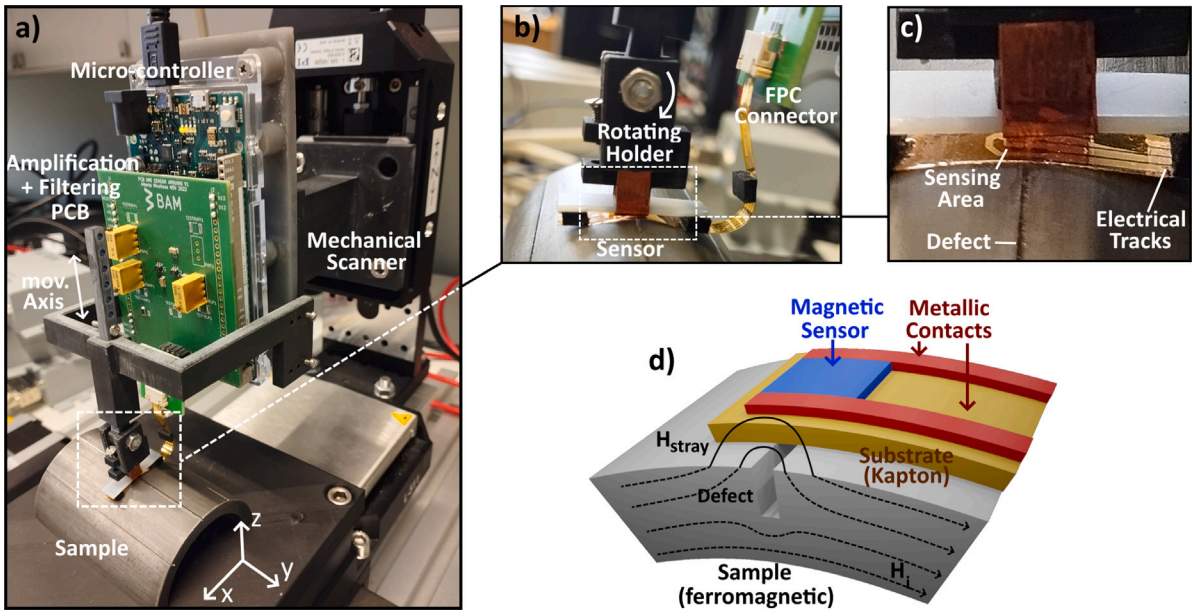

Fig. 3. Sample scanning with flexible AMR sensors: (a) General overview of the scanning setup. A custom-made PCB amplifies and filters the sensor signal. The data is read out by a microcontroller board and transmitted to a computer via serial USB connection. (b) Curved surface scanning: the sensor is attached to a rotating holder capable of adapting to the sample surface during scanning. The connection to the electronics is done via an FPC connector. (c) Detailed view of the conformal shaping of the sensor around the sample. (d) Schematic showing the physics behind magnetic flux leakage scanning: the internal field lines traveling through the ferromagnetic material exit the component in regions where there is a discontinuity in the sample surface, thus making defects detectable by close-range scanning.

These sensors present a sensitive direction perpendicular to the magnetic bars (Fig. 2(c)). Therefore the magnetization orientation of the field to be detected has to be known prior to measurement.

The function of the metallic layer is to connect the magnetic bars electrically in series and provide the connectivity to the electronics. It also consists of tiny oblique barber-poles inclined at a 45° angle on top of the magnetic bars, as shown in Fig. 2(d). These structures have the function of locally redirecting the current flow in such a way as to linearize the sensors around the center-line zero field region [31].

At the end of the thin-film fabrication process, the sensors are encapsulated using a layer of corrosion protection lacquer for printed circuit boards (“Plastik-70”, Kontakt Chemie Germany). This encapsulation therefore reduces the wear and tear from mechanical bending and also protects the sensors from oxidation, making them more durable and more suitable for real life applications.

The sensors were characterized magnetically, electrically and mechanically, as shown in Figs. 2 (e–h).

The magnetic characterization is done for a wide saturation loop (Fig. 2e), showing that the AMR sensor used in this case has a 4-point resistance of 629 Ω with a corresponding magnetoresistance of 1.5%. It can be noticed that the sensor presents some hysteresis characteristic of the barber-pole structure in the sensitive range [6;6] kA/m and saturates outside of it.

Therefore these flexible AMR sensors are useful for detecting weak stray fields emanating from the surface defects. Fig. 2(f) show the magnetic characterization around zero field value, displaying the sensor linearity in the small field region.

Electrical characterization was done by sampling the signal for several DC current values with the sensor exposed to a magnetic field value of 1 kA/m similar to the field amplitude during the scanning shown in section 3.2. A Fourier transform of this data produces the plot shown in Fig. 2(g). At the current of 2.4 mA which is applied to the sensor during the measurements shown in Sections 3.1 and 3.2, the signal is only stable for measurements with a sampling rate above 10 Hz corresponding to measurement times lower than 100 ms.

Mechanical cyclic testing characterization was performed by repeatedly bending the sensor between the radius of 3.4 mm and 3.8 mm. The 4-point resistance of the sensor was measured as a function of time and correlated with the number of bending cycles.

Fig. 2(h) shows the ratio between the sensor resistance and its initial value at maximum and minimum bending radius for every 50 cycles. An acquisition rate of 20 readings per bending period was collected. The inset illustrates the setup used for this measurement. It can be observed that the sensor experiences only a small variation of resistance of the order of 0.3%.

3. Methodology and results

The experimental setup for scanning samples using flexible linear AMR sensors for MFL testing is shown in Fig. 3(a). The flexible sensor is connected to the main PCB via a flexible printed circuit (FPC) connector (Fig. 3(b)). The PCB contains amplification and filtering circuits (Fig. A.1). The resulting signal is then readout by a microcontroller and the data is sent to the computer via a serial USB connection.

The sensor is used as a variable resistor in a voltage divider setup in order to extract the signal. This signal is then amplified by a factor of 270 (48 dB) and filtered by a low-pass filter with a cut-off frequency of 50 Hz in order to eliminate the higher frequency electronic and inductive ambient noise. An external bias offset voltage produced by the digital-to-analog converter (DAC) of the microcontroller is used to center the signal in the region [0;3.3] V, making it readable by the analog-to-digital converter (ADC) of the same.

A voltage divider setup was employed instead of a Wheatstone bridge since direct current (DC) was used in combination with a single sensor. Since only one of the resistive elements is active (the flexible sensor), in a Wheatstone bridge the mid-point of a voltage divider would be measured relative to a fixed reference point, producing similar results. In addition, the employment of the DAC output of the microcontroller to produce the reference voltage allows for the centering of the signal digitally in order not to saturate the ADC input.

The filtering cut-off frequency of 50 Hz was used since most of the detected noise was above this threshold, as shown in Fig. 8 (Section 4). Furthermore, as shown in the same figure, employing a lower cut-off frequency would affect the scanning of larger defects (such as D10) at

Table 1
Dimensions of defects imprinted on the curved sample surface.

Defect	Depth (μm)	Width (μm)	Length (mm)
D1	330	420	70
D2	1100	420	70
D3	2300	420	70

higher scanning speeds. A higher order low-pass filter would further improve the signal quality.

The sensor is sensitive to in-plane magnetic fields along the x-axis. When exposed to external fields along this direction, it produces a variation in its resistivity, which leads to a variation in the voltage readout. It is this variation of the voltage that allows for the detection and mapping of defects. The conversion to magnetic units is done using the slope of the characterization curves shown in Fig. A.3.

The mechanical scanner lands the sensor conformal on the sample surface (Fig. 3(c)). The mechanical holder is designed in such a way that after lowering the scanner to a certain position, the sensor is in contact with the sample surface. Therefore no landing detection is required. Afterwards the computer sends a trigger signal to the microcontroller to start the data acquisition. The sensor is then dragged across the surface in the x direction. At the end of the line-scan, another trigger is sent to stop the data acquisition and collect the data.

Afterwards, the sensor is lifted from the sample surface and returned to the initial position. The scanner moves to the next position in the y direction and the same process of performing a linear scan along the x direction is repeated. In the end, this produces a 2D magnetometer mapping of the sample surface by stacking several line-scans together into a matrix data-set.

The synchronization between the sensor readout process and the movement of the scanner is done via a custom-made user interface developed in Python.

Fig. 3(d) Shows the physics behind stray field detection using these flexible conformal sensors.

3.1. Curved surface scanning

For the purpose of demonstrating the applicability of this type of sensors for curved surface scanning, a semi-cylindrical ferromagnetic steel component was imprinted with 3 reference defects along its surface, with dimensions shown in Table 1. The material of the component is low-carbon steel S235JR. The defects were imprinted on the surface of the sample using a typical drilling process. The sample layout is shown in Fig. 4(a).

The sample magnetization was performed using the device "K+D Universal ACY-700" (K+D Flux-Technic GmbH Co.KG, Germany), shown in Fig. A.2(a). Magnetization was done along the x-axis direction (Fig. A.2(b)) by applying the maximum power of 15 kAW at the coils. After this process, the sample retains a certain amount of remnant magnetization, which leads to the appearance of stray fields emanating from the imprinted defects in its surface. This remnant magnetization has a large longevity, since the sample can retain it for weeks without the need of re-magnetization.

To scan this sample, the sensor is mounted on a rotative holder that also has the ability to move vertically along the z-axis. These two free axes of movement of the holder combined with the gravitational weight maintain the sensor conformal to the curved sample surface during the line-scans along the x-axis. Repeated scans for different positions along the y-axis produce a 2D magnetic mapping. The sensor movement during the scanning of the curved sample is shown in Fig. 4(b–d).

A narrow loop magnetic characterization in the region around 0.2 kA/m (which corresponds to the background field value of the sample) was obtained (Fig. A.3(a)). It can be observed that the sensors present a quasi-linear characterization curve in this narrow region, with a magnetic response of 3 Ω/(kA/m) corresponding to the slope of the fitted line.

These values are used for the conversion of the voltage variation (ΔV) reading into a mapping of the variation of the magnetic field value (ΔkA/m).

In Fig. 4(e) the average center-line signal plot is shown. In this case the signal amplitude is not linearly proportional to the defect depth. One of the reasons for this could be the fact that since the sample has a more complex geometry as compared to the flat sample, the magnetic field within it is more irregular, thus affecting the magnitude of the stray fields emanating from defects. Another reason might be the fact that the lift-off distance of the sensor varies slightly at different positions during scanning, due to the varying normal force applied to the sensor with respect to the sample surface at different positions.

Besides, the sample might not be completely saturated in all regions during magnetization, since it is performed along the x-axis, meaning that only the region around defect D2 is properly magnetized. In the rest of the sample and after magnetization, the internal magnetic field is expected to restructure itself and follow the curvilinear shape of the component, although this ideal case might not correspond to reality.

Therefore, in order to correctly reconstruct the defect depth and geometry, experimental data needs to be correlated with simulations for components with more complex geometries. This might be a subject for future studies.

The resulting magnetometer mapping with area 44 × 3.6 mm^2 is shown in Fig. 4(f). The horizontal white or dark line artifacts represent scans in which the sensor was not perfectly conformal to the sample surface. The scanning resolution is ($\Delta x \times \Delta y$) = (5 × 50 μm^2). A geometrical change between the linear coordinates of the mechanical scanner and the cylindrical coordinates of the sensor was performed in order to reconstruct the stray field mapping with correct positioning, as shown in Fig. A.4.

Figs. 4 (g-i) show the consistency in the profile signal of the defects from the same scan.

3.2. Flat surface scanning

In order to benchmark the performance of these flexible MR sensors, a ferromagnetic steel sample with several reference defects of increasing depth was scanned using both flexible AMR and rigid GMR sensors. The main objective is to compare the SNR of the signal for each defect using both methods. Besides, the effect that defect depth has on the magnitude of the stray fields emanating from them is also studied. The layout of the sample is shown in Fig. 5(a).

The sample has the following dimensions: width = 50 mm; length = 100 mm; height = 9 mm. The material is the same as of the component used in Section 3.1 (low-carbon steel S235JR). The defects were produced using electrical discharge machining (EDM), with depths ranging from 40 μm to 2280 μm. The distance between defects is approximately Δx = 8 mm. To be noted that D6 is a double defect (200 μm spacing between). This small distance between the notches allows for the measurement of the capacity of the sensor to resolute and separate overlapping signals. A detailed list with defect dimensions is shown in the table of Table 2. These values were obtained through microscopic optical depth inspection.

To study the hysteresis and remnant magnetization of the sample material, vibrating sample magnetometer (VSM) characterization of steel powder extracted from the sample material was performed. This was done by measuring a small amount of the steel dust. The results are shown in Fig. 5(b). The inset on the bottom-right side highlights the center-line hysteresis, while the inset on the top-left side shown the remnant magnetization of approximately 2 kA/m.

Stray fields emanating from the defects of this sample were measured using magneto-optical imaging, shown in Figs. 5 (c). This imaging method relies on the change of polarization of light by magnetic fields.

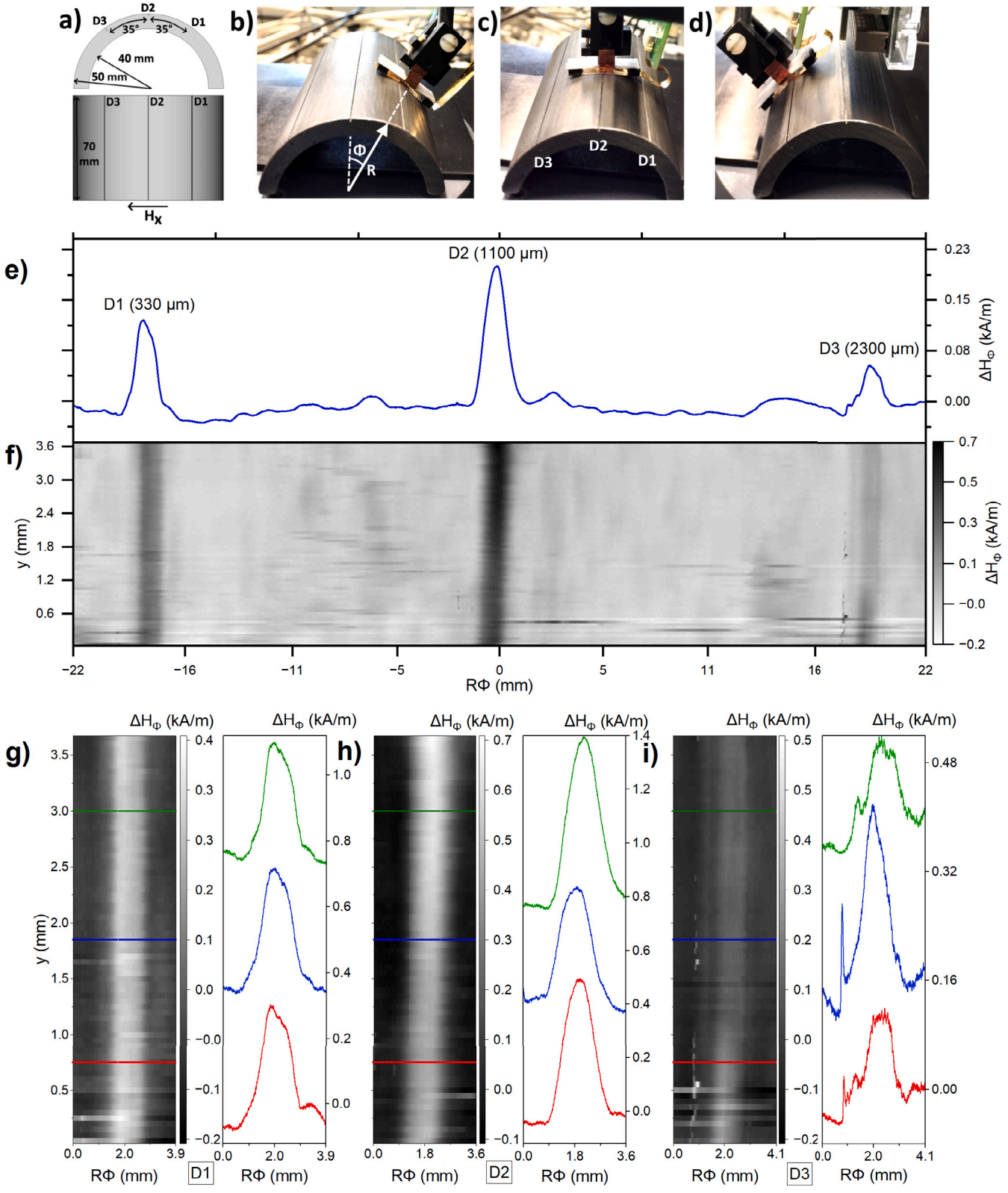

Fig. 4. Scanning of a curved sample with reference defects: (a) Schematic of the sample used, with the positions and dimensions of the 3 defects highlighted. The magnetization direction is shown. (b–d) Showing the movement of the rotative mechanical holder during the scanning process in order to maintain the sensor conformal in-contact with the surface. The cylindrical coordinate system used is also highlighted. (e) Center-line average signal of 70 measurements at different positions of along the y axis, showing the signal amplitude for each defect. (f) 2D magnetometer scanning, after appropriate change to cylindrical coordinates. The scanning step is $(\Delta x \times \Delta y) = (5 \times 50\ \mu m^2)$ before coordinate change. (g–i) The signal profile during individual line-scans consistently demonstrates the profile of each defect.

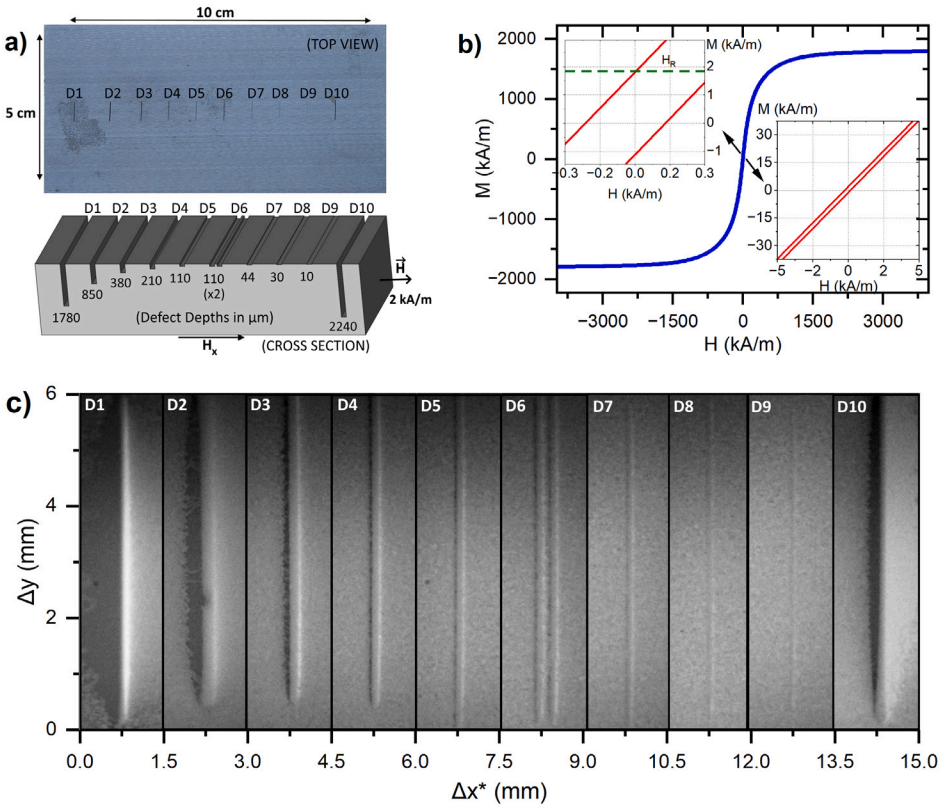

Fig. 5. Overview of the ferromagnetic steel sample used: (a) Top view showing the reference defects that were imprinted on the surface using EDM. Cross-section of the region with reference defects showing the different trench depths. The sample is magnetized along the x-axis. After magnetization a remnant field of 2 kA/m is detected at the poles. Note that D6 is a double defect. (b) The VSM magnetic characterization of the low-carbon steel material of the sample is showing the saturation region. Inset on the bottom-right side highlights the center-line hysteresis. Inset on the top-left side highlights the remnant magnetic field of 2 kA/m after magnetization. (c) Mangeto-optical mapping of the stray fields (ΔH_z) emanating from the defects. (*does not represent the position of consecutive defects; the plots are to be considered separately.).

Table 2
Dimensions of defects imprinted on the flat sample surface.

Defect	Depth (µm)	Width (µm)	Length (µm)
D1	1780	150	5700
D2	850	250	5700
D3	380	190	5700
D4	210	140	5700
D5	110	120	5600
D6a	110	97	5400
D6b	108	95	5400
D7	44	92	5400
D8	30	82	5000
D9	10	81	4800
D10	2240	192	5700

For more shallow defects the SNR ratio is lower, resulting in a more grainy mapping.

The magneto-optical mapping was performed using "Mageye" (Matesy GmbH, Germany). The measurement was done by positioning the magneto-optical sensor covered by a protective foil in-contact with the surface of the sample imprinted with defects.

Prior to magnetometer scanning, the sample was magnetized close to saturation with a DC magnetic field directed along its length (x-axis). The same device and magnetization method as in Section 3.1 was employed (Fig. A.2(c). Similar to the curved sample, the remnant magnetization had a longevity of weeks and produced the stray field emanating from the defects on the sample surface.

Another effect was the appearance of a background magnetic field emanating from the poles due to the remnant magnetization of the sample after this procedure. This field was measured with a Hall probe and has a value of 2 kA/m, corresponding to the remnant magnetization mentioned above.

To a rough approximation, half of the remnant field returns to the opposite pole through the top side of the sample, while the other half returns through the bottom side. This background field can be detected on the surface of the sample, and has a magnitude of the order of 1 kA/m. It overlaps with the stray fields emanating from surface defects, producing a non-linear offset which is eliminated from the experimental data by subtracting a fitting function, as shown in Fig. A.5.

Fig. 6(a) shows the average of the center-line signal of 100 scanned lines from Fig. 6(b). In this case the tangential field component along the x-axis is detected. The sensor is lowered onto the surface and dragged along the sample as shown in Fig. A.6(a). The sensor is maintained in contact with the surface by small plastic pieces. This simple yet effective method produces good results for flat samples.

The full-area 2D magnetometer mapping of the sample surface with an area of 10 × 80 mm^2 and a spatial scanning step of ($\Delta x \times \Delta y$) = (10×50 µm^2) using flexible AMR sensors was obtained - Fig. 6(b) - data shown is the average of 3 scans in order to eliminate the artifacts in certain regions.

The conversion from voltage to magnetic units was performed using the magnetic response (slope) from the narrow loop characterization of the sensor in the range 1 ± 0.4 kA/m. This value was obtained using the same method as in the previous section. The sensor used for this scan presented a base resistance of 487 Ω.

A scanning speed of 10 mm/s with an acquisition rate of 1000 Readings/s was employed, resulting in a full-scan time of 6 h. Higher scanning speeds could be employed, together with higher sampling rates that could decrease this period, as shown in Section 4, where an in-depth analysis of the total scanning time is performed.

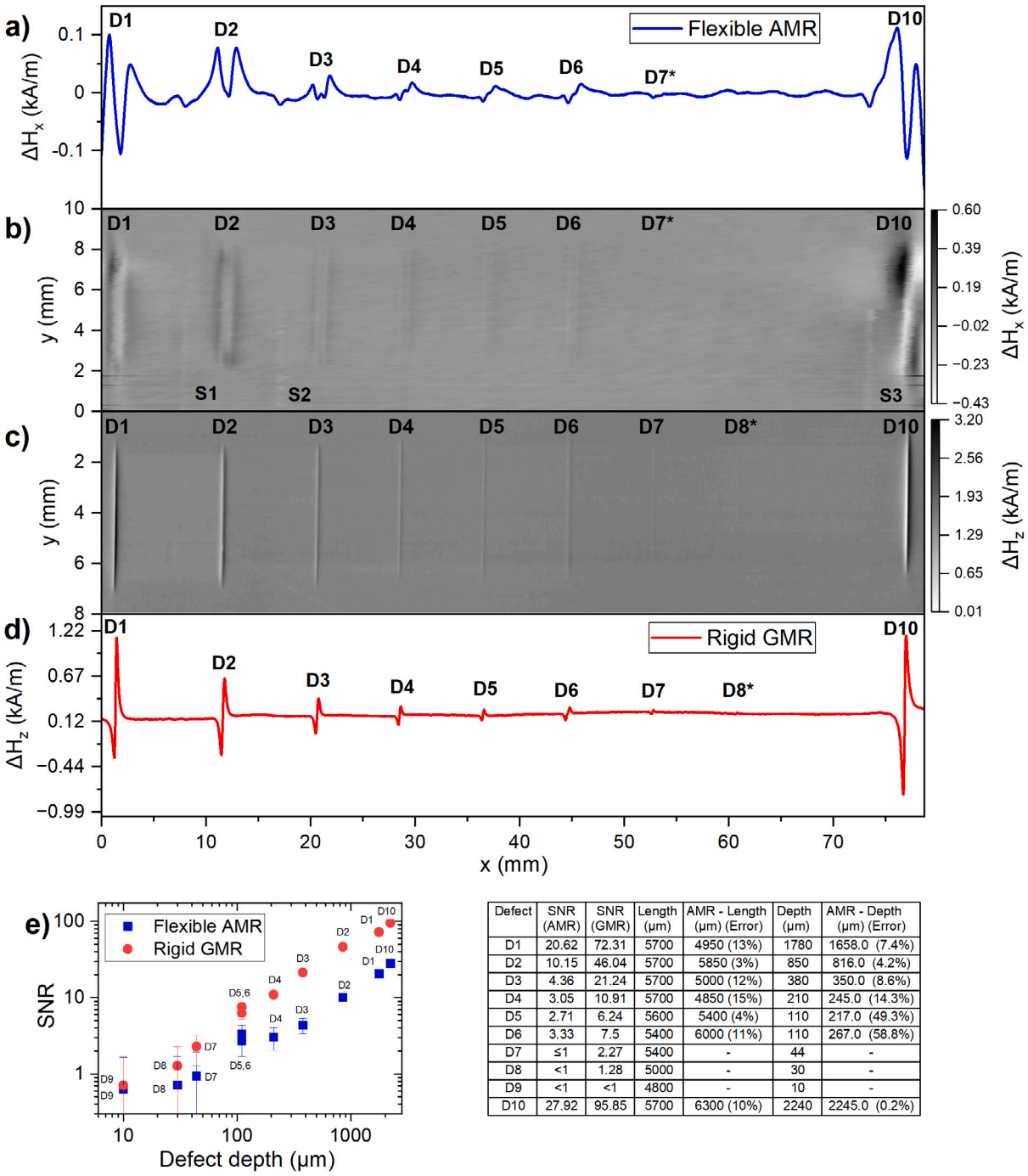

Defect	SNR (AMR)	SNR (GMR)	Length (μm)	AMR - Length (μm) (Error)	Depth (μm)	AMR - Depth (μm) (Error)
D1	20.62	72.31	5700	4950 (13%)	1780	1658.0 (7.4%)
D2	10.15	46.04	5700	5850 (3%)	850	816.0 (4.2%)
D3	4.36	21.24	5700	5000 (12%)	380	350.0 (8.6%)
D4	3.05	10.91	5700	4850 (15%)	210	245.0 (14.3%)
D5	2.71	6.24	5600	5400 (4%)	110	217.0 (49.3%)
D6	3.33	7.5	5400	6000 (11%)	110	267.0 (58.8%)
D7	≤1	2.27	5400	-	44	-
D8	<1	1.28	5000	-	30	-
D9	<1	<1	4800	-	10	-
D10	27.92	95.85	5700	6300 (10%)	2240	2245.0 (0.2%)

Fig. 6. Comparison between the 2D scanning of the reference sample using flexible AMR sensors – magnetometer scan of the in-plane field (a,b) and using rigid GMR sensors – gradiometer scan of the perpendicular magnetic field (c,d) (* at the limit of detection): (a) Leveled plot of the average center-line signal from 100 measurements (line-scans in the region between y = 2 and y = 8 in Fig. b), with the corresponding defects labeled. (b) 2D magnetometer mapping of the tangential magnetic field (ΔH_x) using flexible AMR sensors – scanning step of 10 × 50 μm^2 ($\Delta x \times \Delta y$) – average plot of 3 scans. Surface artifacts (S1, S2, S3) were also detected. (c) 2D magnetometer mapping of the perpendicular magnetic field (ΔH_z) using rigid GMR sensors — scanning step of 16 × 100 μm^2 ($\Delta x \times \Delta y$). (d) Leveled plot of the average center-line signal from 50 measurements of the GMR scan. (e) SNR of the signal amplitude as a function of defect depth for both GMR and AMR scanning (log–log scale). The error bars correspond to SNR = 1, which is the detection threshold. A more detailed SNR list is presented on the table on the right, together with an estimation of defect length and depth (error value in parentheses).

The same scan was performed using rigid GMR sensors, with an area of 8.1 × 90 mm^2 and a spatial scanning step of ($\Delta x \times \Delta y$) = (16 × 100 μm^2). In this case, the perpendicular component of the stray fields along the z-axis is detected. A LO distance of the order of 100 μm was maintained between the sensor and the sample during this scan.

The rigid GMR sensor used is part of a custom-made sensor array of 16 sensors (“GD 709 12A” by Sensitech GmbH, Germany). For this scanning only a single sensor with dimensions of 15 × 25 μm^2 was employed. Fig. A.7 shows the wide loop and narrow loop characterization of the GMR sensor employed. The slope of the curve in the linear region was used for the conversion from voltage to magnetic units.

For flexible AMR scanning, the mechanical oscillations of the sensor as it is dragged across the surface contributes to the signal drift, besides the intrinsic drift of the sensor (presented in Fig. 2(g)). Other factors

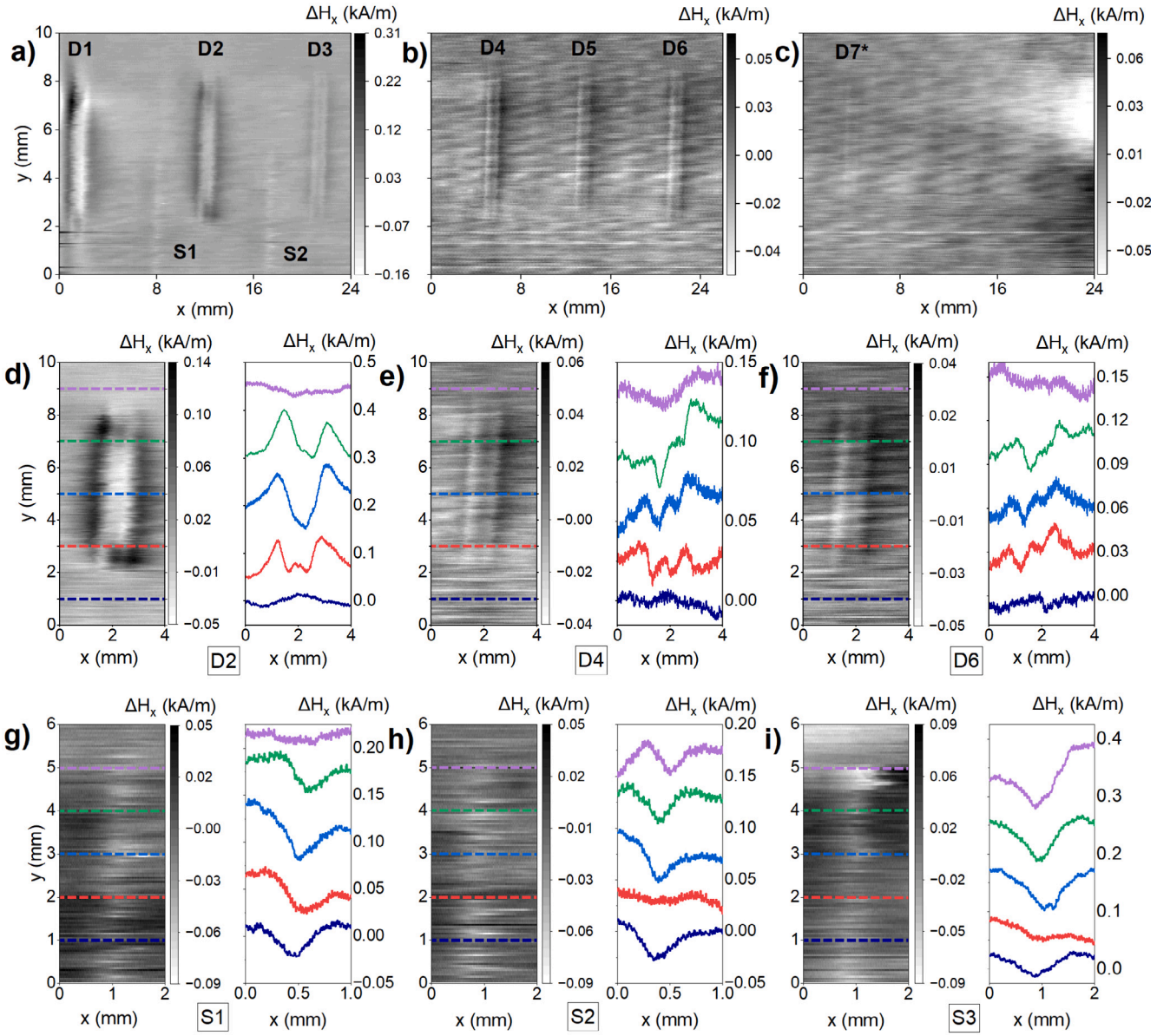

Fig. 7. (a–c) Detailed plots extracted from the 2D magnetometer scan (ΔH_x) shown in Fig. 6 using the appropriate grey-scale adapted to the signal strength of the local defects. (* at the limit of detection). (d–f) Signal comparison of defects D2, D4 and D6. The signal profile is highlighted on the right side for each figure. The center-line signal corresponds to a valley surrounded by two peaks resulting from the in-plane magnetic field inversion at the edge of the defects. (g–i) Profile signal analysis of artifacts S1–S3.

that contribute to the signal drift is the sensor noise and the overall electronic noise of the whole setup, which is filtered but still present. The fact that there is a small but present uncertainty to the landing of the sensor with the method used also induces a tiny uncertainty to positioning of the measurements.

It can be observed that besides detecting the defects (all except D7, D8 and D9 whose SNR is below the noise level), these flexible AMR sensors can also detect artifacts on the surface (S1, S2, S3) as highlighted in Fig. 6(b). The origin of these artifacts is unclear. They might results from surface scratches, subsurface defects or even material imperfections leading to changes in magnetic properties such as permeability. Another cause could be a local change in the LO distance during scanning.

For flexible AMR scanning, defects D1,D2, D3 have a slightly different appearance compared to the more shallow defects (D4–D6) due to the fact that the fitting function applied to linearize the plot does not shift the defects in the center as much since the signal is flatter in that region.

A plot of the SNR as a function of defect depth is shown in Fig. 6(e) using a log–log scale. It can be observed that it follows a quasi-linear relation for both methods employed. The explanation for this phenomenon is that, up to a certain defect depth, the stray field flux density arising from defects is influenced directly by the defect depth, while the variation of width between different defects only stretches these lines along a larger area, thus increasing the signal footprint and not its strength. The same applies to the length of the defects.

A detailed list of the SNR for both methods is shown in table on the right side of the same figure. The estimation of defect length and width is also presented, with the error estimation in parenthesis.

The SNR is considered as being the ratio between the peak-to-peak signal of the averaged center-line signal shown in Fig. 6(a), (d) and the average noise level of each measurement setup. This noise level is measured by taking the average signal dispersion in a region where no defects or major perturbations are present. This way, the entire noise of the setup is taken into consideration, arising from sensor noise together with the electrical and mechanical contributions.

Table 3
Comparison between the advantages and disadvantages of rigid GMR and flexible AMR sensors for MFL testing.

Sensor	Rigid GMR	Flexible AMR
Substrate	Rigid (Silicon)	Flexible (Kapton)
Curved Surface Scanning	Complex setup required	Simple setup needed
Scanning Distance (μm)	100–200	2–20
Minimum detected Depth (μm)	44	110
Maximum SNR (D10)	95.9	27.9

For the scanning with the flexible AMR sensor, it is considered that defects D8 and D9 are not detected since they present a SNR< 1, with D7 at the edge of detection (SNR≈1).

The defect length estimation was obtained by setting a threshold multiple of the SNR. The signal dispersion in each line-scan is then compared with this threshold. For line-scans with amplitude above this value, it is considered that signal from the defect is present and is counted. Finally, the number of line-scans counted is multiplied by the spatial scanning step in the y direction for the corresponding method, resulting in the estimation of the length of the defect.

For depth estimation, a calibration sample was employed in order to extract the slope (magnetic units/μm) which is used for conversion from signal amplitude (kA/m) (Fig. A.8). It can be observed that this quasi-linear model works quite well for deep defects. However, for more shallow defects (D5, D6), this method does not produce accurate results. This can be further improved by employing simulations or a more advanced calibration model.

The estimation of defect width is considered beyond the point of this pilot paper, since the AMR sensors used have a dimension much larger than the defect widths. Ideally for this measurement, the sensors would have to have a dimension below this value. This will be the subject of future studies involving sensor optimization and miniaturization. The sensors employed in this article are not yet optimized for doing a detailed analysis of defect widths.

Different sections of the mapping are highlighted in separate plots with appropriate grey-scale in Fig. 7(a-c). It can also be noticed that the mapping is more noisy for more shallow defects due to their weaker SNR.

The plot with detailed profile signals of defects D2, D4 and D6 obtained from the scanning with flexible AMR sensors is shown in Fig. 7(d-f). It can be observed that the signal profile of every defect presents a valley in the center, surrounded by two peaks, which results from the inversion of the stray magnetic field lines around the edges of defects.

To be noticed that deeper defects have a stronger and more defined signal, while for the more shallow ones the signal is weaker and more noisy. The AMR sensors used could not resolute and separate the signals in the double notches for defect D6 due to the small separation distance relative to the sensor footprint.

In addition, Fig. 7(g-i) highlights the signals originated from the artifacts S1-S3. Their signal profile is similar to the one observed in the reference defects. However, the origin of these artifacts is unclear.

A comparison of the results obtained with flexible AMR and solid GMR sensors is shown in Table 3. Green color represent points in which a certain setup is more advantageous, yellow represents neutrality, while red represents an obvious disadvantage.

4. Scanning speed and noise measurements

To evaluate the filtering efficiency of the data acquisition system used for flexible AMR sensors, the dispersion of the signal as a function of the filtering frequency is evaluated (Fig. 8(a)). A potentiometer mounted on the PCB allows for tuning the low-pass filtering frequency.

It is observed that below the cut-off frequency of 50 Hz, no significant change is observed in the dispersion of the noise amplitude. An acquisition rate of 10 000 Readings/s was used, together with a sampling time of 100 ms, to avoid the signal drift of the sensor (explained in Fig. 3(g)).

In Section 3.2, a high density data set (8000 Readings/line) was obtained to study the performance of the sensors, and a low line scanning speed of 10 mm/s was employed.

However, for practical applications, higher scanning speeds may be necessary. Fig. 8(b) shows that increasing the scanning speed up to 40 mm/s does hardly affect or distort the quality of the signal for defect D10. It is to be noticed that for this maximum speed, the signal amplitude is slightly diminished, possibly a result of the cut-off frequency of 33 Hz interfering with the signal detection itself, since it is obtained at a higher acquisition frequency.

The scanning speed and filtering frequency therefore must be adjusted for optimal results. For high scanning speeds, a higher cut-off frequency is to be employed.

Fig. 8(c) shows line-scans of defect D10 with different sampling densities. It is observed that even for lower sampling rates, the signal is still consistent and well detected. This leads to a decrease in the amount of data to be transmitted during the scans, thus lowering the overall scanning time of the sample.

Part of the scanning time consists of data transmission via USB which is quite slow for the amount of data gathered. The employment of a faster transmission protocol or using a Secure Digital (SD) card reader for the storage of the data in the setup could eliminate this transmission time during scanning. This can be further improved by scanning with a sensor array instead of a single sensor. This will be the subject of future redesigning and optimization.

Fig. 8(d) analyses the Fast Fourier Transform (FFT) of the full line-scan signal at different scanning speeds. It can be observed that most of the signal is collected at frequencies below 5 Hz for the scanning speed of 10 mm/s, considering a threshold of −40 dB corresponding to a 1% change in the signal. However, for the velocity of 20 mm/s this value goes up to 10 Hz, and for 40 mm/s it corresponds to 20 Hz. This is expected since higher acquisition rates are required at larger speeds.

The same process is performed for the data corresponding to the scanning of D10 defect (Fig. 8(e)). It is observed that the signal frequencies go up to 30 Hz when scanning at 40 mm/s. This is due to the fact that it corresponds to the larger signal amplitude amongst all defect, thus inducing the largest signal variation (larger signal slope, corresponding to higher frequencies). Therefore, higher filtering frequencies of the order of 40–50 Hz should be used in this case to avoid signal distortion at large scanning speeds. In both FFT measurements, the data corresponds to 8000 readings/line.

Table 4 analyses the minimum scanning time for the data set with the area of 80 × 10 mm^2 shown in Fig. 6. This analysis is done for different scanning speeds and sampling rates, taking into account the scanning and data transmission times. The minimum scanning time shown excludes any extra movements of the sensors such as landing on the sample and moving from one line-scan to another, since this depends on the method employed and the shape of the sample.

5. Conclusion and outlook

It was demonstrated in Section 3.1 that this type of conformal in-contact scanning using flexible magnetic field sensors has the novel capacity of scanning curved surfaces, without the need of a complex setup. Performing the same process with traditional rigid MR sensors would require a more complicated and more expensive setup, such as a robotic arm, in order to ensure the sensor maintains an optimal distance to the sample surface during the scanning. A rotating setup would only work for cylindrical samples.

In addition, it allows not only for the detection of defects, as it also gives topographical information about the sample surface by detecting material strain regions within the material (regions with changed

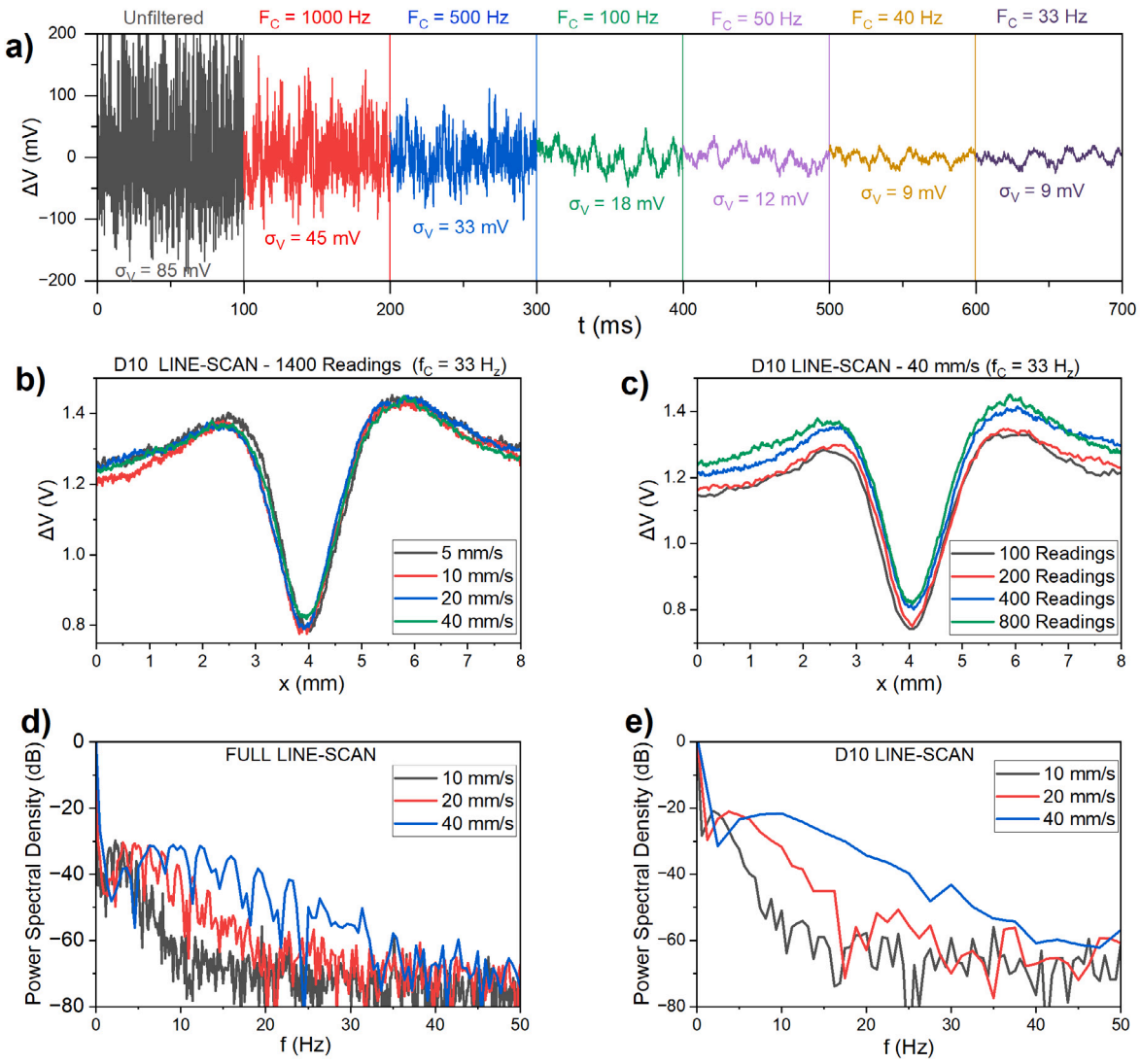

Fig. 8. Scanning time optimization: (a) Filtering characterization: the dispersion of the signal is shown for different filtering frequencies. Scanning data from defect D10 using (b) different scanning speeds and (c) different acquisition densities. (d) Fast Fourier Transform (FFT) of the scanning data for a full line-scan (80 mm, D1–D10) at different scanning speeds. (e) FFT of the scanning data for defect D10 at different scanning speeds.

Table 4
Minimum total scanning time for a flat area of 80 × 10 mm^2 at different scanning speeds and sampling rates per line-scan. (*)This total scanning time does not include extra movements of the scanner such as landing on the sample.

Readings/line	Step (Δx) (μm)	Step (Δy) (μm)	Scan. Time/line (s)	Transm. Time/line (s)	Min. Scan. Time* (min)
1000	80	50	8	7.5	52
2000	40	50	8	15	77
4000	20	50	8	30	127
8000	10	50	8	60	227
1000	80	50	4	7.5	38
2000	40	50	4	15	63
4000	20	50	4	30	113
8000	10	50	4	60	213
1000	80	50	2	7.5	32
2000	40	50	2	15	57
4000	20	50	2	30	107
8000	10	50	2	60	207

magnetic properties). This is mainly due to the fact that the scanning distance is equal to the substrate thickness, making this method very sensitive to weak close-range stray fields.

The performance of these novel AMR sensors was then benchmarked in comparison to standard rigid GMR sensors. The SNR comparison between the two methods shows that defects with depth down to

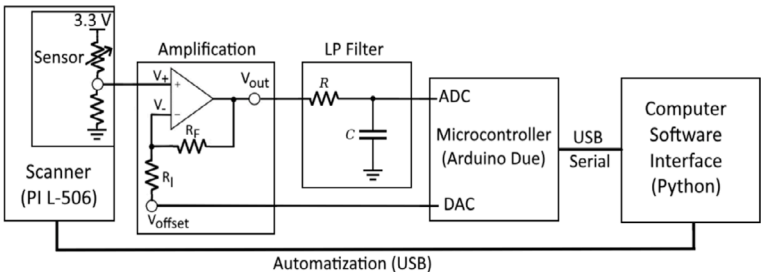

Fig. A.1. Electrical schematic — the flexible sensor acts as a variable resistor in a voltage divider setup. The signal is amplified, filtered and read by a microcontroller. A software interface developed in Python synchronizes the movement of the scanner with the sensor readout by sending a trigger signal to the microcontroller at the beginning of each linear scan.

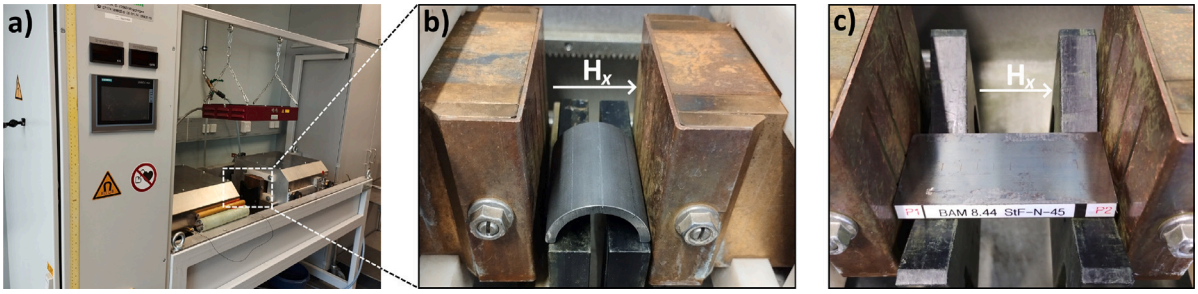

Fig. A.2. Magnetization method: (a) "K+D Universal ACY-700" (GmbH Co.KG, Germany) was used to magnetize the samples. (b) Magnetization of the curved sample scanned in Section 3.1. (c) Magnetization of the flat sample scanned in Section 3.2.

110 μm can be detected with SNR down to the value of 3.3 in the case of tangential scanning using flexible AMR sensors and with an SNR of 7.5 in the case of perpendicular scanning using rigid GMR sensors, while more shallow defects are not detectable using flexible AMR sensors. Despite the fact that GMR sensors are capable of detecting shallower defects, other types of features, such as material changes, were only detectable by the flexible AMR sensors.

In conclusion, the performance of the employed flexible AMR sensors closely approaches that of the rigid GMR sensors used, despite being one order of magnitude less sensitive.

This method of dragging the sensor along the sample surface was not harmful to the sensor since it is positioned on the top side of the substrate and covered in a protective plastic layer, therefore not exposed to friction or any mechanical pressure. Furthermore, the substrate itself does not appear to be affected by friction during scanning, since hundreds of line-scans were performed during this study without producing a change in the performance and characteristics of the sensor.

The durability of the sensor for thousands of line-scans is yet to be tested. A thin protective layer can also be sprayed on the bottom of the substrate to ensure additional durability. An alternative type of polymer foils with higher durability can also be used.

It is also worth mentioning that the flexible AMR sensor width is much larger than the defect width, leading to a lower SNR than if the sensor had more reduced dimensions of the order of the defects. This is because the sensor signal results from the average field beneath its surface.

Therefore, due to the size of the sensors, the width measurement of the defects is not accurate. The defects appear to have a width of the order of 1 mm (which corresponds to the sensor dimensions) instead of approximately 200 μm which is the real geometrical value.

Further miniaturization and optimization of the flexible MR sensor design is needed in order to improve sensor resolution. Next steps will also involve developing arrays and matrices of sensors in order to speed up the scanning process and increase the applicability of this setup.

CRediT authorship contribution statement

Alberto Nicolicea: Writing – review & editing, Writing – original draft, Visualization, Validation, Software, Methodology, Investigation, Formal analysis, Data curation, Conceptualization. **Eduardo Sergio Oliveros-Mata:** Validation, Writing – review & editing. **Yevhen Zabila:** Resources. **Denys Makarov:** Project administration, Resources, Supervision, Writing – review & editing. **Michael Melzer:** Conceptualization, Funding acquisition, Project administration, Resources, Supervision, Validation, Writing – review & editing. **Matthias Pelkner:** Conceptualization, Funding acquisition, Project administration, Resources, Supervision, Validation, Writing – review & editing.

Declaration of competing interest

The authors declare that they have no conflict of interest.

Data availability

Data will be made available on request.

Acknowledgments

The authors of this article acknowledge the discussion and the help with AMR sensor fabrication with Dr. Gilbert Santiago Canon Bermúdez, Pavlo Makushko and Conrad Schubert from the Helmholtz-Zentrum Dresden-Rossendorf (HZDR).

This research work was funded in the framework of the BAM-internal funding instrument "Menschen – Ideen; Ideen: Entwickeln" ("People - Ideas; Ideas: Develop").

This work is also financially supported via the European Union's Horizon Europe Research and Innovation Programme, Grant Agreement # 101070066 (project REGO) and via the German Research Foundation (DFG) grant MA 5144/28-1.

Appendix

See Figs. A.1–A.8.

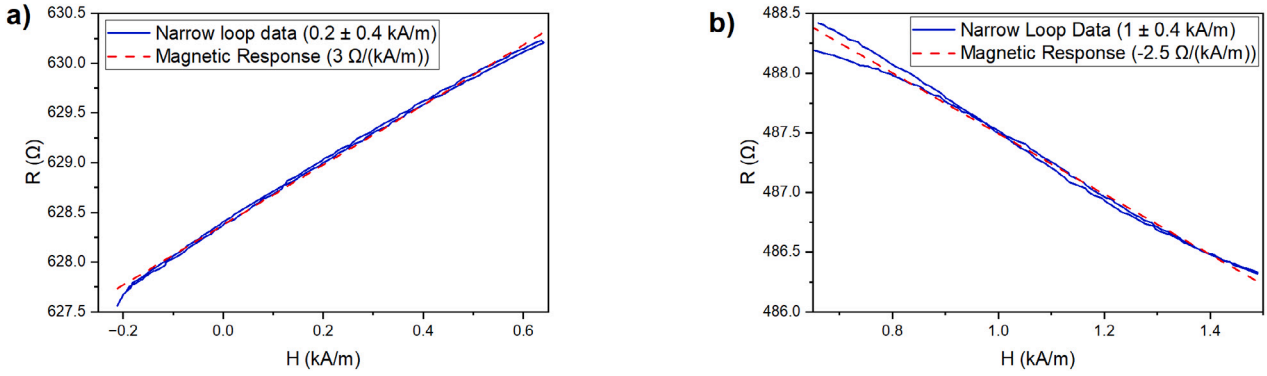

Fig. A.3. Magnetic response characterization: (a) Magnetic characterization of the sensor used in section 3.1 for the region 0.2 ± 0.4 kA/m; a quasi-linear behavior is observed, with the slope corresponding to the magnetic response of the sensor. (b) Magnetic characterization of the sensor used in section 3.2 for the region 1 ± 0.4 kA/m. The slope (magnetic response) was used for voltage to magnetic unit conversion.

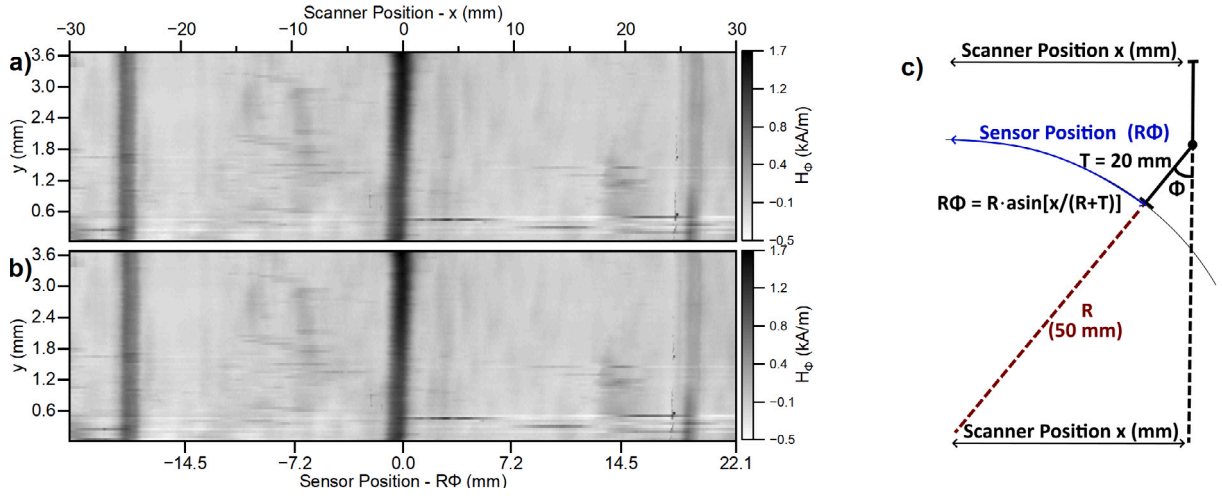

Fig. A.4. Illustration of the method used for coordinate changes in the case of curved sample scanning: (a) Before the change of coordinates. (b) After change to cylindrical coordinates. (c) Sketch of the function used. To be noticed that a huge change is not observed in the mapping due to the small angle involved (±35°).

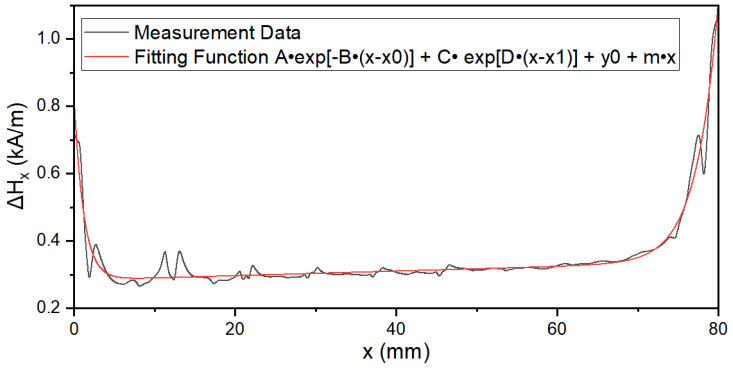

Fig. A.5. Demonstration of the fitting method used to subtract the background field from the data of the flat sample scanning. To be noted that the 1 kA/m offset between the center and the edges, corresponding to the background field crossing the top section of the sample.

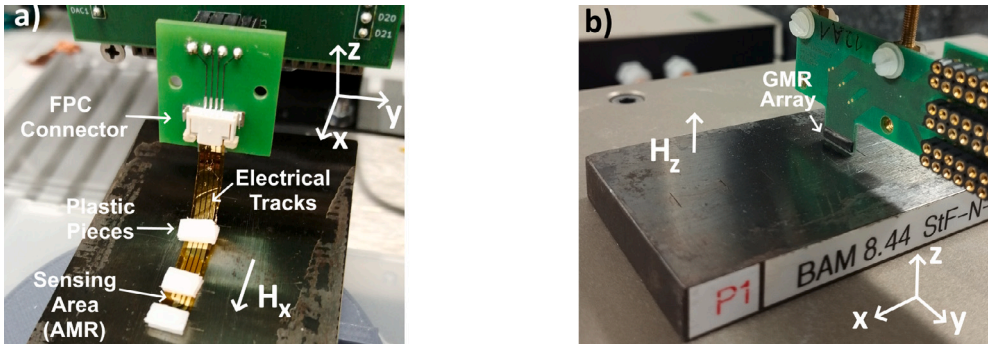

Fig. A.6. Flat surface scanning: (a) The flexible magnetic sensor is simply dragged along the flat sample surface, being held down by gravity from the weight of the plastic pieces. The field component H_x is detected. (b) Rigid GMR scanning setup: a sensor from a GMR array is used to detect the field H_z emanating from defects.

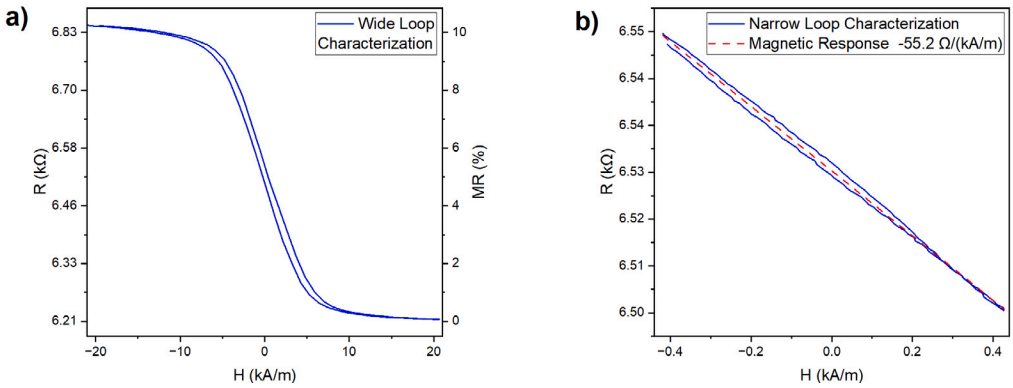

Fig. A.7. GMR sensor characterization: (a) Wide characterization loop showing the sensitive region in the center. (b) Narrow loop around zero field value showing the linear region, with the slope of the curve corresponding to the magnetic response value.

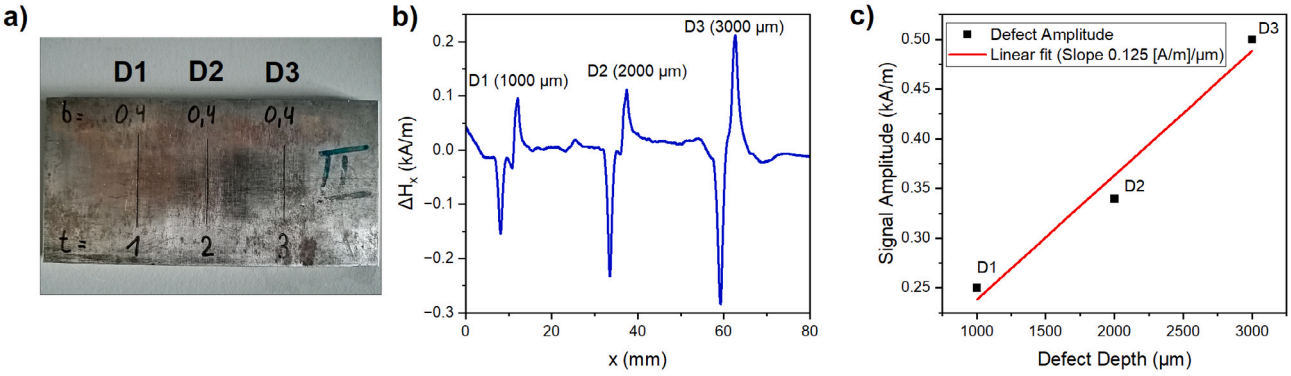

Fig. A.8. Measurements for depth calibration (Flexible AMR): (a) Calibration sample with 3 reference notches. (b) Signal amplitudes of the reference defect (average of 200 scans). An amplification factor of 200 (43 dB) was used here. (c) Linear fit to obtain the slope used in the depth measurements.

References

[1] Gholizadeh S. A review of non-destructive testing methods of composite materials. Procedia Struct Integr 2016;1:50–7. http://dx.doi.org/10.1016/j.prostr.2016.02.008.

[2] Jiles DC. Review of magnetic methods for nondestructive evaluation (Part 2). NDT Int 1990;23(2):83–92. http://dx.doi.org/10.1016/0308-9126(90)91892-W.

[3] Feng B, Wu J, Tu H, Tang J, Kang Y. A review of magnetic flux leakage nondestructive testing. Materials 2022;15:7362. http://dx.doi.org/10.3390/ma15207362.

[4] Sun Yanhua, Kang Yihua. Magnetic mechanisms of magnetic flux leakage nondestructive testing. Appl Phys Lett 2013;103:184104. http://dx.doi.org/10.1063/1.4828556.

[5] Yang L, Zhang G, Liu G. Effect of lift-off on pipeline magnetic flux leakage inspection. 17th world conference on nondestructive testing, Shanghai, China, 25–28 Oct 2008. e-J Nondestruct Test 2008;13(11). https://www.ndt.net/?id=6674.

[6] Chang Yu, Jingpin Jiao, Li Guanghai, Liu Xiucheng, He Cunfu, Wu Bin. Effects of excitation system on the performance of magnetic-flux-leakage-type nondestructive testing. Sensors Actuators A 2017;268. http://dx.doi.org/10.1016/j.sna.2017.08.009.

[7] Li Yong, Ward Steve. Numerical simulation on magnetic flux leakage evaluation at high speed. NDT & E Int 2006;39:367–73. http://dx.doi.org/10.1016/j.ndteint.2005.10.006.

[8] Wu Qiang, Dong Kang, Qin Xunpeng, Hu Zeqi, Xiong Xiaochen. Magnetic particle inspection: Status, advances, and challenges — Demands for automatic nondestructive testing. NDT & E Int 2024;143:103030. http://dx.doi.org/10.1016/j.ndteint.2023.103030.

[9] Baumeyer Julien, Chatoux Hermine, Pelletier Arnaud, Marquié Patrick. Industrial application of AI-based assistive magnetic particle inspection. Appl Sci 2024;14:1499. http://dx.doi.org/10.3390/app14041499.

[10] Sharatchandra Waikhom, Bhagi Purna Chandra, Vaidyanathan S, Jayakumar T, Raj Baldev. Detection of leakage magnetic flux from near-side and far-side defects in carbon steel plates using a giant magneto-resistive sensor. Meas Sci Technol 2007;19:015702. http://dx.doi.org/10.1088/0957-0233/19/1/015702.

[11] Deng Zhiyang, Sun Yanhua, Kang Yihua, Song Kai, Wang Rongbiao. A permeability-measuring magnetic flux leakage method for inner surface crack in thick-walled steel pipe. J Nondestruct Eval 2017;36. http://dx.doi.org/10.1007/s10921-017-0447-z.

[12] Guo D, Cardoso Filipe, Ferreira R, Paz Elvira, Cardoso Susana, Freitas Paulo. MgO-based magnetic tunnel junction sensors array for non-destructive testing applications. J Appl Phys 2014;115. http://dx.doi.org/10.1063/1.4863933.

[13] Zheng Chao, Zhu Prewitt K, Cardoso Susana, Chang Jen-Yuan, Davies Joseph, Eames Peter, et al. Magnetoresistive sensor development roadmap (Non-recording applications). IEEE Trans Magn 2019;1–30. http://dx.doi.org/10.1109/TMAG.2019.2896036.

[14] Cubells-Beltrán M-D, Reig C, Madrenas J, De Marcellis A, Santos J, Cardoso S, et al. Integration of GMR sensors with different technologies. Sensors 2016;16:939. http://dx.doi.org/10.3390/s16060939.

[15] Reimund Verena, Pelkner Matthias, Kreutzbruck Marc, Haueisen Jens. Sensitivity analysis of the non-destructive evaluation of micro-cracks using GMR sensors. NDT & E Int 2014;64. http://dx.doi.org/10.1016/j.ndteint.2014.02.003.

[16] Pelkner Matthias, Neubauer Andreas, Reimund Verena, Kreutzbruck Marc, Schütze Andreas. Routes for GMR-sensor design in non-destructive testing. Sensors 2012;12:12169–83. http://dx.doi.org/10.3390/s120912169.

[17] Pelkner Matthias, Reimund Verena, Erthner Thomas, Kreutzbruck Marc. Size adapted GMR arrays for the automated inspection of surface breaking cracks in roller bearings. Int J Appl Electromagn Mech 2014;45:473–9. http://dx.doi.org/10.3233/JAE-141866.

[18] Sharatchandra Waikhom, Stegemann R, Kreutzbruck Marc, Mukhopadhyay CK, Bhagi Purna Chandra. Mapping of deformation-induced magnetic fields in carbon steels using a GMR sensor based metal magnetic memory technique. J Nondestruct Eval 2018;37. http://dx.doi.org/10.1007/s10921-018-0470-8.

[19] Sharatchandra Waikhom, Stegemann R, Kreutzbruck Marc. Three-dimensional finite element analysis of the stress-induced geometry effect on self-magnetic leakage fields during tensile deformation. Insight, Non-Destr Test Cond Monit 2016;58. http://dx.doi.org/10.1784/insi.2016.58.10.544, 544-550(7).

[20] Stegemann Robert, Cabeza Sandra, Lyamkin Viktor, Bruno Giovanni, Pittner Andreas, Wimpory R, et al. Residual stress characterization of steel TIG welds by neutron diffraction and by residual magnetic stray field mappings. J Magn Magn Mater 2016;426. http://dx.doi.org/10.1016/j.jmmm.2016.11.102.

[21] Reimund Verena, Blome Mark, Pelkner Matthias, Kreutzbruck Marc. Fast defect parameter estimation based on magnetic flux leakage measurements with GMR sensors. Int J Appl Electromagn Mech 2011;37:199–205. http://dx.doi.org/10.3233/JAE-2011-1391.

[22] Stegemann Robert, Cabeza Sandra, Pelkner Matthias, Lyamkin Viktor, Pittner Andreas, Werner Daniel, et al. Influence of the microstructure on magnetic stray fields of low-carbon steel welds. J Nondestruct Eval 2018;37. http://dx.doi.org/10.1007/s10921-018-0522-0.

[23] Sharatchandra Waikhom, Bhagi Purna Chandra, Nand K, Thirunavukkarasu Sannasi, Jayakumar T, Raj Baldev. Magnetic flux leakage Nde using Giant Magneto-Resistive (GMR) sensors. AIP Conf Proc 2008;975. http://dx.doi.org/10.1063/1.2902753.

[24] Pelkner Matthias, Blome Mark, Reimund Verena, Thomas H-M, Kreutzbruck Marc. Flux leakage measurements for defect characterization using a high precision 3-AXIAL GMR magnetic sensor. AIP Conf Proc 2011;1335:380–7. http://dx.doi.org/10.1063/1.3591878.

[25] Pelkner Matthias, Neubauer A, Reimund Verena, Kreutzbruck Marc. Local magnetization unit for GMR array based magnetic flux leakage inspection. AIP Conf Proc 2012;1430:1005–12. http://dx.doi.org/10.1063/1.4716332.

[26] Zhong X, Zhang X. Non-destructive testing of steel wire rope using magnetic flux leakage: Principle, sensor design and signal wavelet analysis. Int J Simul Syst, Sci Technol 2016;17. http://dx.doi.org/10.5013/IJSSST.a.17.26.26.

[27] Kim Ju-Won, Park Seunghee. Magnetic flux leakage sensing and artificial neural network pattern recognition-based automated damage detection and quantification for wire rope non-destructive evaluation. Sensors 2018;18. http://dx.doi.org/10.3390/s18010109.

[28] Park Seunghee, Kim Ju-Won, Lee Changgil, Lee Jong Jae. Magnetic flux leakage sensing-based steel cable NDE technique. Shock Vib 2014;2014:1–8. http://dx.doi.org/10.1155/2014/929341.

[29] Saha Shilpi, Mukhopadhyay Sudarsan, Mahapatra U, Bhattacharya S, Srivastava Gautam. Empirical structure for characterizing metal loss defects from radial magnetic flux leakage signal. NDT & E Int - NDT E INT 2010;43:507–12. http://dx.doi.org/10.1016/j.ndteint.2010.05.006.

[30] Javed Ali, Sadeghnejad Amir, Rehmat Sheharyar. Magnetic Flux Leakage (MFL) method for damage detection in internal post-tensioning tendons. 2022.

[31] Usarek Zbigniew, Warnke K. Inspection of gas pipelines using magnetic flux leakage technology. Adv Mater Sci 2017;17. http://dx.doi.org/10.1515/adms-2017-0014.

[32] Mukhopadhyay CK, Sharatchandra Waikhom, Bhagi Purna Chandra. Development of a high sensitive magnetic flux leakage instrument for imaging of localised flaws in small diameter ferromagnetic steel tubes. IET Sci, Meas Technol 2018;12. http://dx.doi.org/10.1049/iet-smt.2018.5201.

[33] Chen L, Que P-W, Jin Tao. A giant-magnetoresistance sensor for magnetic-flux-leakage nondestructive testing of a pipeline. Russ J Nondestruct Test 2005;41:462–5. http://dx.doi.org/10.1007/s11181-005-0193-7.

[34] Sharatchandra Waikhom, Bhagi Purna Chandra, Thirunavukkarasu Sannasi, Jayakumar T. Flexible GMR sensor array for magnetic flux leakage testing of steel track ropes. J Sensors 2012;2012. http://dx.doi.org/10.1155/2012/129074.

[35] Melzer Michael, Karnaushenko Daniil, Makarov Denys, Baraban Larysa, Calvimontes Alfredo, Mönch Ingolf, et al. Elastic magnetic sensor with isotropic sensitivity for in-flow detection of magnetic objects. RSC Adv 2012;2:2284–8. http://dx.doi.org/10.1039/C2RA01062C.

[36] Melzer Michael, Kaltenbrunner Martin, Makarov Denys, Karnaushenko Dmitriy, Karnaushenko Daniil, Sekitani Tsuyoshi, et al. Imperceptible magnetoelectronics. Nat Commun 2015;6:6080. http://dx.doi.org/10.1038/ncomms7080.

[37] Makarov Denys, Melzer Michael, Karnaushenko Daniil, Schmidt Oliver. Shapeable magnetoelectronics. Appl Phys Rev 2016;3:011101. http://dx.doi.org/10.1063/1.4938497.

[38] Melzer Michael, Mönch Jens, Makarov Denys, Zabila Yevhen, Bermudez Gilbert, Karnaushenko Daniil, et al. Wearable magnetic field sensors for flexible electronics. Adv Mater (Deerfield Beach, Fla.) 2015;27. http://dx.doi.org/10.1002/adma.201405027.

[39] Bermúdez Gilbert, Fuchs Hagen, Bischoff Lothar, Fassbender Jürgen, Makarov Denys. Electronic-skin compasses for geomagnetic field-driven artificial magnetoreception and interactive electronics. Nat Electron 2018;1:589–95. http://dx.doi.org/10.1038/s41928-018-0161-6.

[40] Bermúdez Gilbert, Karnaushenko Dmitriy, Karnaushenko Daniil, Lebanov Ana, Bischoff Lothar, Kaltenbrunner Martin, et al. Magnetosensitive e-skins with directional perception for augmented reality. Sci Adv 2018;4:eaao2623. http://dx.doi.org/10.1126/sciadv.aao2623.

[41] Ha Minjeong, Bermúdez Gilbert, Liu Jessica, Oliveros Mata Eduardo Sergio, Evans Benjamin, Tracy Joseph, et al. Reconfigurable magnetic origami actuators with on-board sensing for guided assembly. Adv Mater 2021;33. http://dx.doi.org/10.1002/adma.202008751.

[42] Mishurova Tatiana, Stegemann Robert, Lyamkin Viktor, Cabeza Sandra, Evsevleev Sergei, Pelkner Matthias, et al. Subsurface and bulk residual stress analysis of S235JRC + C Steel TIG weld by diffraction and magnetic stray field measurements. Exp Mech 2022;62. http://dx.doi.org/10.1007/s11340-022-00841-x.

[43] Pelkner Matthias, Stegemann Robert, Sonntag Nadja, Pohl R, Kreutzbruck Marc. Benefits of GMR sensors for high spatial resolution NDT applications. AIP Conf Proc 2018;1949:040001. http://dx.doi.org/10.1063/1.5031535.

[44] Krishnan Kannan. Fundamentals and applications of magnetic materials. 2016, http://dx.doi.org/10.1093/acprof:oso/9780199570447.001.0001, [Chapter 6].